2023 IEEE International Conference on Robotics and Automation (ICRA 2023)
May 29 - June 2, 2023. London, UK

Optimal Workpiece Placement Based on Robot Reach, Manipulability and Joint Torques

Baris Balci[1], Jared Donovan[1], Jonathan Roberts[1], and Peter Corke[1]

***Abstract*— Workpiece placement with respect to an industrial robot plays an important role in robotic manufacturing due to its influence on the configuration-dependent properties of industrial robots. Suboptimal placements of the workpiece may increase the required joint torques and decrease the dexterity of the robot. The focus of this work is to identify an optimal workpiece pose that enables a robot to carry out surface finishing with configurations that require the lowest possible joint torques while having maximum possible manipulability. We present a non-linear optimization-based algorithm to solve this problem and demonstrate the algorithm's capability on different workpieces which we share to facilitate further research in this area.**

I. INTRODUCTION

As the manufacturing paradigm shifts from mass manufacturing to flexible manufacturing, the ability to manufacture different products using existing equipment increases competitive advantage. With their precision, payload capacity and large workspace, industrial robots became critical equipment since they can be utilized for different sorts of applications. Machining and surface finishing, which are generally carried out with CNC machines or manual labour, are two applications that are moving into the robotics domain.

Machining and surface finishing operations require material removal from a workpiece to achieve the desired shape and surface smoothness. The material is removed by moving a cutting or abrasive tool along predefined toolpaths. During travel, these tools both exert and experience forces due to their contact with the workpiece. The precision in toolpath following, and consistency in force application, directly determine the quality of the final product. Multi-axis CNC machines provide great precision and high stiffness, however, their high cost and limited workspace make them difficult to use in flexible manufacturing [1]. Industrial robots are seen as a possible solution to the shortcomings of CNC systems, but they introduce their own challenges.

Maintaining precise motions under external forces is challenging for industrial robots because of their posture-dependent stiffness [2], [3]. Since many kinematic and dynamic properties of industrial robots depend on their configuration, the placement of a workpiece relative to the robot plays a crucial role in the success of a material removal operation. Typically a trial and error approach is used to find a placement that is able to generate products that satisfy quality criteria. The financial and operational costs of manual workpiece placement may be tolerable for relatively static mass-manufacturing scenarios, however, in flexible manufacturing operations that are frequently changing, these costs may become burdensome.

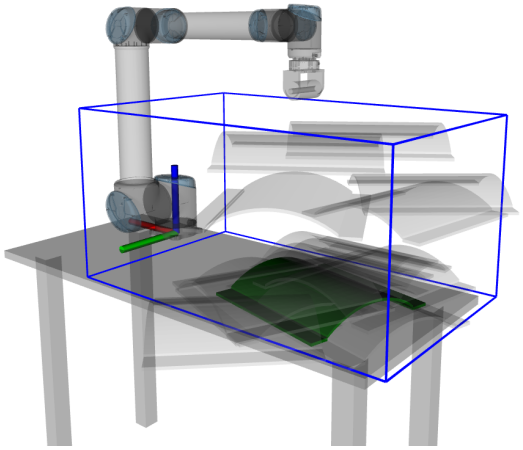

Fig. 1: A representation of the workpiece placement problem in a bounded workspace. The transparent and green workpieces display the intermediate and final results of the proposed algorithm, respectively. The robot base frame, $\{\mathrm{B}\}$, is represented by red, green and blue unit vectors, which correspond to the X, Y and Z axes, respectively.

The contribution of this paper are:

- a novel cost function that considers robot manipulability, required joint torques and operational parameters that can be used in optimization to determine optimal workpiece pose as shown in Fig. 1.
- a publicly shared set of benchmark workpiece objects that will support reproducible research in this area.

II. RELATED WORK

Different approaches have been investigated to increase the performance of industrial robots in material removal operations. A notable feature of much of this prior work is that it has focussed on robot stiffness, since it is the main cause of issues in robotic material removal operations. Caro et al. [4] proposed a solution to find the optimal workpiece placement by posing it as an optimization problem with the objective of minimizing the end-effector deflections from the targeted task-space poses. The deflections were calculated using the Cartesian stiffness values of a KUKA KR270-2 robot. Liao et al. [5] presented a method that solves an optimization problem with an objective to increase stiffness using workpiece and end-effector orientation for 5-axis milling

[1]Australian Cobotics Centre, Queensland University of Technology, Brisbane, 4000, Queensland, Australia. All correspondence should be addressed to baris.balci@hdr.qut.edu.au

[2]https://github.com/bbalci/wp_optimizer

tasks. The approach was extended to complex workpieces which require a significant robot configuration change while following trajectories, by proposing a surface segmentation algorithm that ensures each segment satisfies a minimum stiffness value. Gotlih et al. [6] used a combination of genetic algorithm and non-linear optimization to find optimal deburring paths. In their approach, the genetic algorithm was used to find the best object pose by maximizing the robot stiffness through the deburring path, while the non-linear optimization ensured the toolpaths were reachable and continuous.

Liao et al. [7] maximized stiffness in the normal direction of the surface poses, moreover, their approach also determined an optimized feed direction for the different regions on the workpiece to maximize the stiffness in the tangential direction. Chen et al. [8] also investigated the effect of stiffness in robotic milling operations, but their study also focused on how the orientation of the end-effector may affect the deflection in the normal direction during a milling operation.

Lin et al. [9] determined an operation region in the robot workspace using a manipulability-based kinematic performance index and the stiffness properties of the robot. The approach was validated by a hole-drilling test in which a workpiece in a feasible region yields fewer deflections compared to a workpiece in a non-feasible region. Janez et al. [10] optimized the robot configuration for manipulability, structural inertia, damping ratios and natural frequencies, in addition to the stiffness.

A disadvantage of the above approaches is that obtaining the stiffness values of a robot is not a trivial process, as it would require additional sensors [11]. Researchers have also demonstrated approaches based on components other than stiffness, such as velocities, reachability, manipulability and robot joint limitations.

Nektarios and Aspragathos [12] optimized the location of the robot for generating maximum task-space velocity with minimum joint velocities. Similarly, Stradovnik and Hace [13] introduced a new approach, which maximizes available translational and rotational velocities of the tool center point (TCP) of an industrial robot during task execution. Xia et al. [14] generated a kinematic performance map based on a kinetostatic condition index that was used to optimize robot configurations. The relation between the kinetostatic condition index through a toolpath and the object's orientation in yaw axis was also investigated.

Vosniakos and Matsa [15] presented the idea of jointly optimizing for high manipulability and low joint torques for milling applications. The optimization was implemented with a two-step genetic algorithm optimization approach. The kinematic and dynamic manipulability of poses in a milling path were maximized in the first step. In the second step, the total joint torques of the three most dominant joints that are required to generate the desired wrench were minimized. Weingartshofer et al. [16] introduced a custom index for robot base placement optimization that consists of four components: number of inverse kinematics solutions, number of solutions that yield continuous paths, joint motion minimization and distance from the joint limits.

Malhan et al. [17] presented a workpiece placement algorithm that ensures multiple constraints required for the robotic operation are met. After an evaluation of the workspace of the robot in terms of reach and manipulability, a non-linear optimizer was used to find a workpiece pose that has the lowest violation cost, a metric that is based on the pose errors due to defined tolerances for the TCP axes.

While the use of these alternative components has been shown to be viable in the literature, the problem remains that an entire workspace evaluation or mapping for these properties may be computationally expensive. An approach similar to the one that Vosniakos and Matsa proposed, that focuses on the optimization of the crucial properties directly may eliminate the need of investigating the entire workspace.

III. PROBLEM DEFINITION

The goal of our work is to find an optimal workpiece pose, with respect to the robot base, for surface finishing operations – we denote that pose ${}^{B}\xi_{W} \subset \mathbb{R}^3 \times (S^1)^3$. Surface finishing requires the finishing paths to be followed with high precision along with consistent force application. To meet these requirements all of the robot configurations during the task should have high dexterity and be capable of generating the required forces. An optimal ${}^{B}\xi_{W}$ allows the robotic setup to reach all required surfaces on the workpiece while respecting operational constraints with minimum effort.

A Universal Robots UR10 which has six degrees of freedom is considered in this paper. The robot is equipped with a grinding wheel and the TCP is defined on the outer surface of the wheel. To carry out the surface finishing operation, the robot needs to make the TCP travel along a toolpath, $\mathcal{P}$, which consists of n poses that lay on the surface of the workpiece. Each pose, ${}^{W}\xi_{i} \in \mathcal{P}, i \in 1, \ldots, n$ is defined with respect to frame $\{\mathrm{W}\}$, which represents the center of a bounding box that encloses the workpiece. The TCP and each ${}^{W}\xi_{i}$ for a workpiece are shown in Fig. 2.

The joint configuration of the robot $\boldsymbol{\theta} \in \mathbb{R}^6$ is calculated using inverse kinematics for each pose in $\mathcal{P}$

$$\boldsymbol{\theta}_i = \mathcal{K}^{-1}\left({}^{B}\xi_{W} \oplus {}^{W}\xi_{i}\right)$$

to visit all of the poses on the workpiece. The existence of an inverse kinematics solution depends highly on the workpiece pose ${}^{B}\xi_{W}$. An inverse kinematic solution for every ${}^{W}\xi_{i}$ is necessary, but not sufficient, for a successful surface finishing operation. The properties of each robot configuration require further investigation in terms of manipulability, collisions and joint constraints to be considered a valid configuration.

Manipulability

$$m(\boldsymbol{\theta}) = \sqrt{\det\left(\mathbf{J}(\boldsymbol{\theta})\,\mathbf{J}^{\top}(\boldsymbol{\theta})\right)} \tag{1}$$

indicates how dexterous a robot is at a given configuration by determining how far it is away from singularities. Manipulability is calculated using the geometric Jacobian matrix, $\mathbf{J} \in \mathbb{R}^{6\times 6}$, for the configuration, $\boldsymbol{\theta}$ [18].

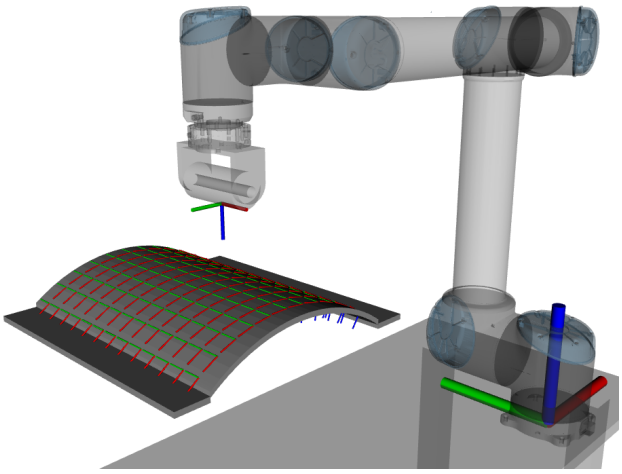

Fig. 2: The defined TCP on the grinding wheel and the ${}^{W}\xi_i$ on the workpiece. The TCP and ${}^{W}\xi_i$ frames are represented by red, green and blue unit vectors, which correspond to the X, Y and Z axes, respectively.

When the robot is in a singular configuration, the manipulability value is equal to 0 and the value increases as the robot configuration moves away from the singularity. Thus, finding a ${}^{B}\xi_W$, which leads to ${}^{W}\xi_i$ that correspond to robot configurations with high manipulability ensures that the robot never reaches a singular configuration and stays dexterous during task execution.

The attached grinding wheel needs to be in contact with the workpiece to remove material but the wheel must be the only part of the robotic setup to be in contact with the workpiece. Robot configurations that yield any other interaction of the robot with its own structure or the workpiece cause collisions and must be avoided to protect the robot and the workpiece from any damage.

The robot joint limits should also be taken into account while evaluating the validity of a robot configuration. Both physical joint-angle limits and joint-torque limits should be respected to make sure that the TCP can reach the desired poses and apply desired forces.

For surface finishing operation with a grinding wheel, the grinding wheel's axis of rotation determines the axis that the robot needs to move the tool along. During the motion, the robot needs to exert a force, f_n, in the direction of the surface normals of ${}^{W}\xi_i$ and withstand f_t, the tangential force that is in the opposite direction of the tool motion. In abrasive operations, the relation between f_n and f_t is defined as $f_t = \mu f_n$, where μ is the *force ratio* and is reported to be generally between 0.2 and 0.7 [19]. The wrench $\boldsymbol{w} = [f_x, f_y, f_z, m_x, m_y, m_z]^\top$ represents forces and moments acting on the TCP. The corresponding components of $\boldsymbol{w}$ for f_n and f_t depends on the definition of ${}^{W}\xi_i$ and the tool design.

The required joint torques are

$$\boldsymbol{\tau} = \mathbf{J}_{TCP}^{\top}(\boldsymbol{\theta})\, \boldsymbol{w} \tag{2}$$

where $\boldsymbol{\tau} \in \mathbb{R}^6$ is the required joint torques and $\mathbf{J}_{TCP} \in \mathbb{R}^{6\times 6}$ is the geometric Jacobian matrix which is defined with respect to the TCP. The same wrench $\boldsymbol{w}$ can be obtained at different configurations as long as the calculated joint torques are below the joint torque limits. Finding a configuration that would generate a wrench using lower joint torques is key since it would allow the robot to have the joint torque budget to increase the applied forces if needed and resist unexpected changes in external forces during surface finishing.

The outcome of surface finishing operations can be improved by identifying robot configurations for each pose on the workpiece which can apply a wrench with minimal joint torques while having maximum manipulability. Each unique pose of the workpiece would change the properties of the robot configurations for each ${}^{W}\xi_i$, therefore a workpiece placement procedure is needed to achieve the best configuration properties.

IV. PROPOSED APPROACH

For any ${}^{B}\xi_W$, manipulability and required joint torques for each pose on the workpiece can be easily calculated using (1) and (2). However, determining robot configurations that simultaneously achieve high manipulability and lower required joint torques to apply a certain wrench is not trivial. We use a multivariate non-linear optimizer to determine an optimal workpiece pose, ${}^{B}\xi^{*}_W$, that lead to such configurations.

We perform constrained optimization

$$\begin{aligned} {}^{B}\xi^{*}_W = \arg\min_{{}^{B}\xi_W} \quad & f\,({}^{B}\xi_W) \\ \text{s.t.} \quad & \mathcal{K}^{-1}\,({}^{B}\xi_W \oplus {}^{W}\xi_i) \neq \emptyset \\ & c = 0 \\ & \boldsymbol{\theta}_{min} \leq \boldsymbol{\theta} \leq \boldsymbol{\theta}_{max} \\ & [\,{}^{B}\xi_W]_t \subset \mathcal{W} \end{aligned} \tag{3}$$

which minimizes the cost function while respecting four constraints. There must be a $\boldsymbol{\theta}_i$ for each ${}^{W}\xi_i$, the number of collisions, c, must be zero, the physical joint-angle limits ($\boldsymbol{\theta}_{min}$, $\boldsymbol{\theta}_{max}$) must not be violated and the translational component of the workpiece pose $[\,{}^{B}\xi_W]_t$ must be kept within the bounds of the workspace $\mathcal{W}$. Keeping the workpiece in these bounds is realized by the utilized optimizer and the rest are checked in the cost function.

Our cost function

$$f({}^{B}\xi_W) = \begin{cases} \alpha \frac{1}{m_{min}} + r_{max} & \text{if } v = 0 \\ \\ 10^6 & \text{if } v \geq 1 \end{cases} \tag{4}$$

where v is the violation count, the number of times that the remaining constraints are violated. For zero violations the function penalizes low manipulability (m_{min}) and high joint torque (r_{max}) over all the tool poses for the workpiece pose ${}^{B}\xi_W$. The two components of the cost function are unitless but their dynamic ranges differ so a parameter α is introduced to balance the contribution of the components.

In order to compute m_{min} and r_{max} we first require $\boldsymbol{\theta}_i$ for each ${}^{W}\xi_i$. After obtaining a $\boldsymbol{\theta}_i$, the joint limits are checked and the robot configuration is tested for collisions using the workpiece's CAD model. Inverse kiematic failure, $\boldsymbol{\theta}_i$

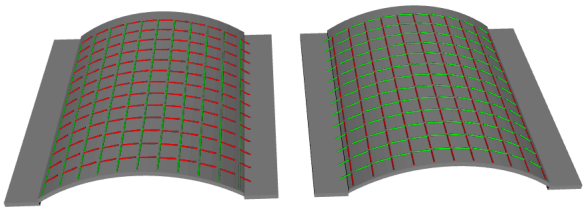

Fig. 3: Different surface finishing directions on the same workpiece. In the considered setup, the paths are followed in the direction of +Y-axis, which is represented by green unit vectors.

that violates joint limits or causes collision are individually considered violations.

For manipulability we consider the minimum manipulability over the path

$$m_{min} = \min_{i=1,\dots,n} m(\boldsymbol{\theta}_i) \tag{5}$$

and the optimization problem (3) will attempt to maximize this – keeping the robot as dextrous as possible.

For joint torques we consider the maximum relative joint torque required over the path

$$r_{max} = \max_{i=1,\dots,n} \max_{j=1,\dots,6} \frac{|\tau_j|}{\bar{\tau}_j} \tag{6}$$

where τ_j and $\bar{\tau}_j$ are respectively the joint torque and the maximum permissible joint torque for the j^{th} joint. This ensures that all joint torques are kept below their maximum value.

Non-linear optimizers could generate global or local solutions depending on their implementation. Global optimizers can avoid local extrema at the expense of greater computation times, on the other hand, local optimizers can return a solution faster but the solution is not guaranteed to be the best in the search space. Since the optimizer we use is a local one, we propose an algorithm that introduces a structure around the local optimizer to address its shortcomings.

The first component of the algorithm is the surface finishing direction that is dictated by the way the poses on the workpiece are defined. If the workpiece pose is kept constant and a rotation is applied to the poses on the workpiece about their individual surface normals, the surface finishing direction would change. This rotation can be given to the optimizer as an input along with the workpiece pose at the expense of increasing the computational cost of the optimizer. To avoid that, the surface finishing directions that should be considered by the optimization algorithm need to be decided beforehand. For each surface finishing direction, all the poses in $\mathcal{P}$, are rotated about their surface normal by the desired amount and treated as a new path, $\mathcal{P}'$. Two identical workpieces with different surface finishing directions specified are shown in Fig. 3.

Due to the nature of local optimizers, a single optimization run for an arbitrary ${}^{B}\xi_W$ in the bounded workspace may not result in an optimal pose for the workpiece. The second component of the algorithm focuses on this matter. To

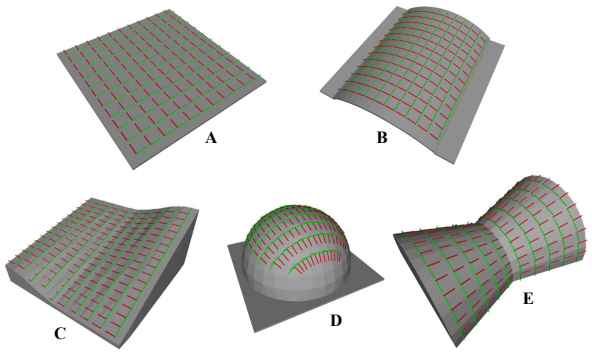

Fig. 4: The publicly shared benchmark workpieces that are used in the tests of the proposed algorithm.

increase the possibility of finding an ideal ${}^{B}\xi_W$, the optimizer must be enabled to explore multiple regions in the bounded workspace. We form l seed poses, ${}^{B}\xi'_{Wk}, k \in 1,\dots,l$ \$ across the bounded workspace to address this issue. The optimizer runs for each seed pose and returns a solution, ${}^{B}\xi^{*}_{Wk}$. The ${}^{B}\xi^{*}_{Wk}$, which generates the minimum cost when given to the cost function is considered as the optimal pose for the workpiece, ${}^{B}\xi^{\circ}_{W}$. The seed poses are generated with randomized position and orientation components within the bounds of the workspace. The cost function is run once for each seed pose to check that it does not violate any constraints. The ones that are in violation are replaced. Randomization in the seed poses exposes the optimizer to different conditions and the violation check increases the possibility of finding a valid workpiece pose. If the algorithm is evaluating multiple surface finishing directions, l seed poses are created for each surface finishing direction.

V. RESULTS

The proposed algorithm was tested under a simulation environment with five different workpieces, that differ from each other in terms of curvature and number of ${}^{W}\xi_i$. The workpieces are shown in Fig. 4. The toolpaths of workpieces A, B, C, D and E contain 121, 143, 164, 155 and 140 poses, respectively. The search space of the algorithm is limited by the bounded workspace. The workspace is defined as a rectangular prism with 1m depth, 0.6m width and 0.5m height. Although, the optimizer is capable of taking all components of a ${}^{B}\xi_W$ as an input, for this paper only the translational components and the yaw orientation of workpiece pose are used.

In the considered robot setup, the grinding wheel rotates about the X-axis of the TCP, and the ${}^{W}\xi_i$ are followed towards the +Y-axis of the TCP. In this scenario, f_t is experienced towards the -Y-axis of the TCP. To withstand that, the robot needs to be able to generate the same amount of force in the opposite direction. The surface normals of ${}^{W}\xi_i$ point in the same direction as the Z-axis of the TCP, thus f_n is exerted in the +Z-axis of the TCP. For testing, we only considered the forces that are acting on the TCP by setting the f_n to 50N and the aforementioned μ to 1 to test for extreme conditions. To represent the grinding wheel

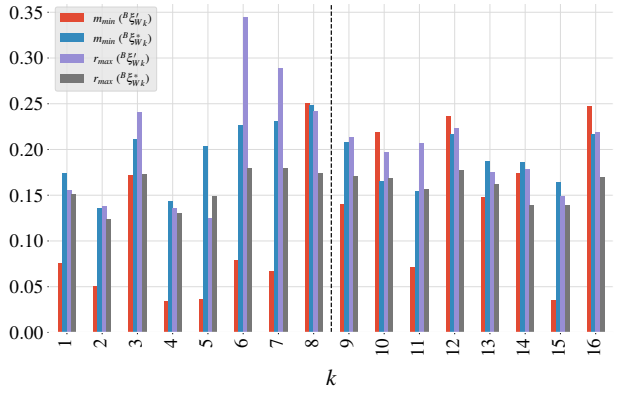

Fig. 5: m_{min} and r_{max} values before and after seed pose optimization for workpiece A

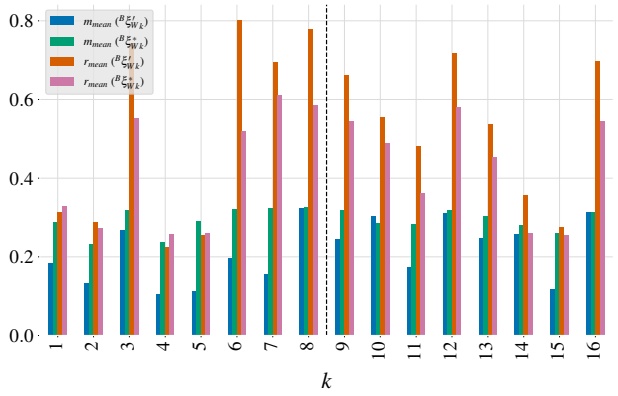

Fig. 6: m_{mean} and r_{mean} values before and after seed pose optimization for workpiece A

TABLE I: Average relative changes in m_{min} and r_{max} after the same eight seed poses are optimized with different α values for workpiece B

α	$\Delta\ m_{min}$	$\Delta\ r_{max}$
1.0	370.43%	0.89%
0.1	314.23%	7.62%
0.01	210.18%	-26.38%
0.001	44.53%	-49.68%

forces a wrench of $\boldsymbol{w} = [0, 50, 50, 0, 0, 0]^\top$ is applied at the TCP.

Before running the algorithm on the workpieces, the effect of the α on the optimizer is investigated. For workpiece B, eight random seed poses, ${}^{B}\xi'_{Wk}$, are generated for one surface finishing direction. While keeping the seed poses the same, the algorithm is run with different α values to generate, ${}^{B}\xi^{*}_{Wk}$. Relative changes in the m_{min} and r_{max} from ${}^{B}\xi'_{Wk}$ to ${}^{B}\xi^{*}_{Wk}$ are observed for each α. Table I shows the average relative changes in the m_{min} and r_{max} between the seed poses and their optimized results. For greater α values, the optimizer can yield significantly increased m_{min}, but the r_{max} does not decrease. On the other hand, when α is too low, it jeopardizes the m_{min} optimization. For our experiments, we choose α to be 0.01 since this value allows the optimizer to realize the desired behaviour.

After determining α, two polishing directions are investigated and eight random seed poses are generated for each polishing direction to find the optimal pose, ${}^{B}\xi^{\circ}_{W}$, for each workpiece. For the first surface finishing direction, each ${}^{W}\xi_i$ is left as it is, and for the second direction, each ${}^{W}\xi_i$ is rotated $\pi/2$ rad about its surface normal (Z-axis).

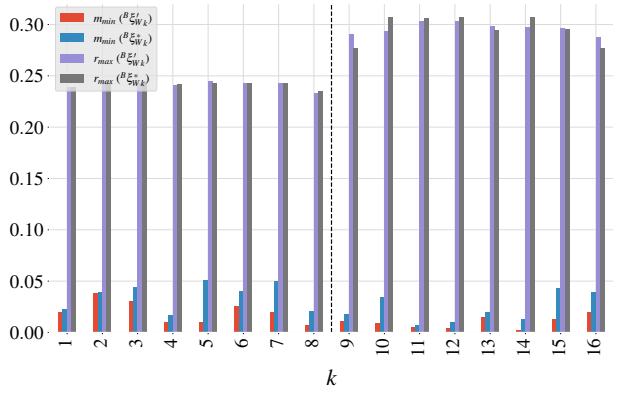

Fig. 7: m_{min} and r_{max} values before and after seed pose optimization for workpiece D

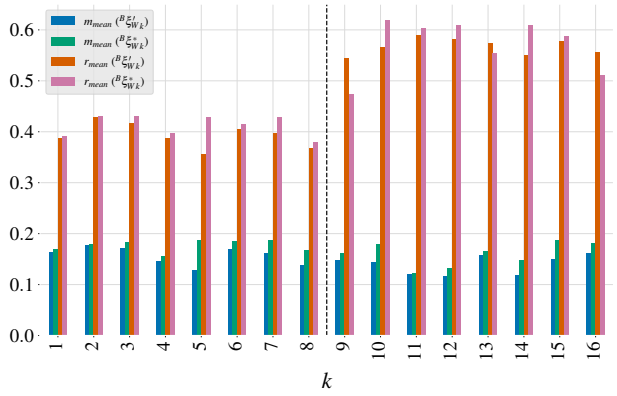

Fig. 8: m_{mean} and r_{mean} values before and after seed pose optimization for workpiece D

The results are analyzed in two steps. The first step is a check on the non-linear optimizer. The optimizer is expected to decrease the calculated cost for each seed pose by increasing m_{min} and decreasing the r_{max}. The second step is a comparison between the seed pose with the lowest cost, ${}^{B}\xi'^{,min}_{W}$ and the optimal pose, ${}^{B}\xi^{\circ}_{W}$. This comparison shows how much of an improvement can be achieved by the algorithm.

m_{min} and r_{max} are the main parameters to consider during evaluation due to their explicit effect on the cost function. To analyze the implicit effects of the algorithm, the mean manipulability, m_{mean}, and total absolute relative torques, r_{sum}, and the mean of the total absolute relative torques, r_{mean} over each $\mathcal{P}$ are also examined.

$$m_{mean} = \sum_{i=1}^{n} \frac{m(\boldsymbol{\theta}_i)}{n} \quad (7) \qquad r_{sum} = \sum_{j=1}^{6} \frac{|\tau_j|}{\bar{\tau}_j} \quad (8) \qquad r_{mean} = \sum_{i=1}^{n} \frac{r_{sumi}}{n} \quad (9)$$

Figures 5 and 7 display m_{min} and r_{max}, while Figures 6 and 8 display m_{mean} and r_{mean} for seed poses and their optimization result for workpieces A and D. The first eight

TABLE II: The relative change in m_{min}, m_{mean}, r_{max} and r_{mean} between ${}^{B}\xi_{W}^{\prime,min}$ and ${}^{B}\xi_{W}^{\circ}$ for all workpieces

Workpiece	$\Delta\, m_{min}$	$\Delta\, m_{mean}$	$\Delta\, r_{max}$	$\Delta\, r_{mean}$
A	6.9%	8.9%	-21.93%	-29.50%
B	33.36%	4.46%	-28.49%	-36.79%
C	-8.21%	-1.29%	-22.28%	43.86%
D	33.24%	5.15%	-1.0%	1.95%
E	0.84%	2.98%	-25.66%	-18.82%

TABLE III: Total seed pose optimization times for each workpiece

	A	B	C	D	E
Time (min)	20.9	34.3	27.0	32.33	26.9

seed poses belong to the first surface finishing direction and the rest belong to the second. When the figures are examined, it can be seen that the cost minimization occurred in different ways for these two workpieces. For workpiece A, the optimizer managed to increase m_{min} and decrease r_{max} at the same time for most of the seed poses. In general, the optimization also indirectly increased m_{mean} and decreased r_{mean} for workpiece A. On the other hand, for workpiece D, the cost minimization was mostly realized as a result of the increase in m_{min}. The reason for no change in r_{max} could be related to the selected α value. While working with seed poses with significantly low m_{min}, lower α values can help the optimizer to lower r_{max}.

The algorithm determines the optimal pose, ${}^{B}\xi_{W}^{\circ}$, by selecting the, ${}^{B}\xi_{W\,k}^{*}$, that generates the minimum cost after seed pose optimization. To analyze the performance of this approach we compare the determined optimal pose, ${}^{B}\xi_{W}^{\circ}$, to the seed pose with the lowest cost, ${}^{B}\xi_{W}^{\prime,min}$. In this comparison, the seed pose with the lowest cost demonstrates a good random workpiece placement. Table II presents the relative changes in m_{min}, m_{mean}, r_{max} and r_{mean} between ${}^{B}\xi_{W}^{\prime,min}$ and ${}^{B}\xi_{W}^{\circ}$. Except for workpiece C, the ${}^{B}\xi_{W}^{\circ}$ for each workpiece have better m_{min} and r_{max} than the ${}^{B}\xi_{W}^{\prime,min}$. In the case of workpiece C, the algorithm offers a ${}^{B}\xi_{W}^{\circ}$ with lower r_{max} and lower m_{min}. This issue can be resolved using a greater α value for workpiece C. Figures 9 and 10 display histograms of all m and r_{sum} of ${}^{B}\xi_{W}^{\prime,min}$ and ${}^{B}\xi_{W}^{\circ}$ along their respective toolpaths on workpiece B. The algorithm-generated pose, ${}^{B}\xi_{W}^{\circ}$, both increase m_{min} and m_{mean} by shifting all m towards the greater end of the graph in Fig. 9. In Fig. 10, the r_{sum} of ${}^{B}\xi_{W}^{\circ}$ that clustered on the lower end side of the graph shows that the algorithm has the capability of lowering the total required joint torques.

Table III presents the total time spent on the seed pose optimization for each workpiece. The time that the optimization requires is directly related to the volume of the bounded workspace, the shape of the workpiece, the number of polishing directions, the number of ${}^{W}\xi_{i}$ and the number of components of the ${}^{B}\xi_{W}$ that are used for optimization. All of these elements except the shape of the workpiece can be chosen in a way that lowers the required time, however, this may result in missing some optimal workpiece poses.

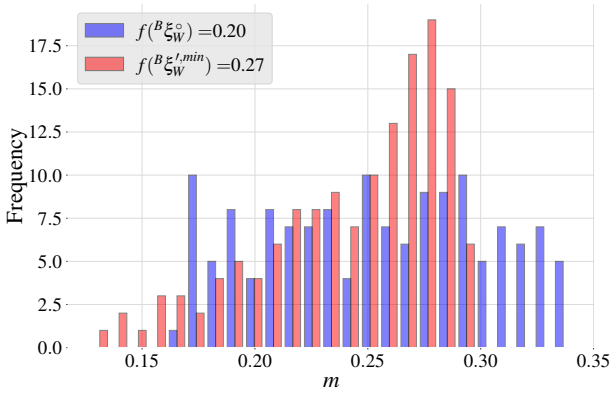

Fig. 9: Histogram of m of ${}^{B}\xi_{W}^{\circ}$ and ${}^{B}\xi_{W}^{\prime,min}$ (Workpiece B)

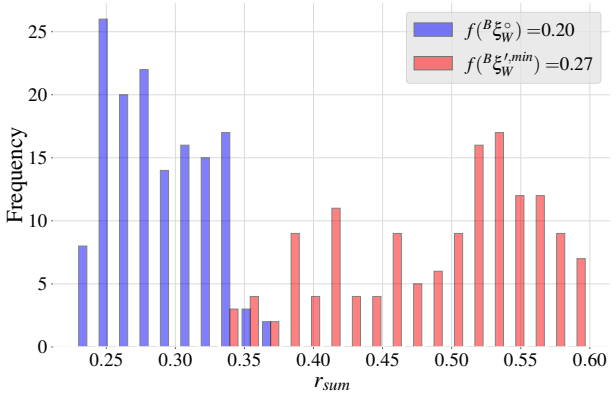

Fig. 10: Histogram of r_{sum} of ${}^{B}\xi_{W}^{\circ}$ and ${}^{B}\xi_{W}^{\prime,min}$ (Workpiece B)

VI. CONCLUSION

In this work, a non-linear optimization-based algorithm is presented to determine an optimal workpiece pose with respect to the robot base to improve robotic surface finishing operations. Instead of evaluating the entire workspace, multiple regions of a bounded workspace are investigated using random seed poses and the workpiece pose is optimized to lead robot configurations that can apply a wrench with the lowest possible joint torques while having maximum possible manipulability. During the optimization, the effect of the surface finishing direction is also considered and the robot constraints are respected. The algorithm was tested on five different workpieces in a simulation environment and the presented results showed that the algorithm yielded a more optimal workpiece pose compared to random poses.

ACKNOWLEDGMENT

This study was supported by The Industrial Transformation Training Centre (ITTC) for Collaborative Robotics in Advanced Manufacturing (also known as the Australian Cobotics Centre) funded by ARC (Project ID: IC200100001) and a Department of Industry, Innovation and Science (Innovative Manufacturing CRC Ltd.) UAP Australia Pty Ltd co-funded project grant "Design Robotics for Mass Customisation Manufacturing" (IMCRC/UAP/25072017).

REFERENCES

[1] D. Zhu, X. Feng, X. Xu, Z. Yang, W. Li, S. Yan, and H. Ding, "Robotic grinding of complex components: A step towards efficient and intelligent machining – challenges, solutions, and applications," *Robotics and Computer-Integrated Manufacturing*, vol. 65, Oct. 2020.

[2] W. Ji and L. Wang, "Industrial robotic machining: a review," *International Journal of Advanced Manufacturing Technology*, vol. 103, pp. 1239–1255, June 2019.

[3] Y. Chen and F. Dong, "Robot machining: Recent development and future research issues," *International Journal of Advanced Manufacturing Technology*, vol. 66, pp. 1489–1497, June 2013.

[4] S. Caro, C. Dumas, S. Garnier, and B. Furet, "Workpiece placement optimization for machining operations with a kuka kr270-2 robot," *Proceedings - IEEE International Conference on Robotics and Automation*, pp. 2921–2926, 2013.

[5] Z. Y. Liao, Q. H. Wang, H. L. Xie, J. R. Li, X. F. Zhou, and P. Hua, "Optimization of robot posture and workpiece setup in robotic milling with stiffness threshold," *IEEE/ASME Transactions on Mechatronics*, vol. 27, pp. 582–593, Feb. 2022.

[6] J. Gotlih, M. Brezocnik, and T. Karner, "Stiffness-based cell setup optimization for robotic deburring with a rotary table," *Applied Sciences (Switzerland)*, vol. 11, Sept. 2021.

[7] Z. Y. Liao, J. R. Li, H. L. Xie, Q. H. Wang, and X. F. Zhou, "Region-based toolpath generation for robotic milling of freeform surfaces with stiffness optimization," *Robotics and Computer-Integrated Manufacturing*, vol. 64, Aug. 2020.

[8] C. Chen, F. Peng, R. Yan, Y. Li, D. Wei, Z. Fan, X. Tang, and Z. Zhu, "Stiffness performance index based posture and feed orientation optimization in robotic milling process," *Robotics and Computer-Integrated Manufacturing*, vol. 55, pp. 29–40, Feb. 2019.

[9] Y. Lin, H. Zhao, and H. Ding, "Posture optimization methodology of 6r industrial robots for machining using performance evaluation indexes," *Robotics and Computer-Integrated Manufacturing*, vol. 48, pp. 59–72, Dec. 2017.

[10] G. Janez, K. Timi, G. Karl, and B. Miran, "Accuracy improvement of robotic machining based on robot's structural properties," *International Journal of Advanced Manufacturing Technology*, vol. 108, pp. 1309–1329, May 2020.

[11] C. Dumas, S. Caro, S. Garnier, and B. Furet, "Joint stiffness identification of six-revolute industrial serial robots," *Robotics and Computer-Integrated Manufacturing*, vol. 27, pp. 881–888, Aug. 2011.

[12] A. Nektarios and N. A. Aspragathos, "Optimal location of a general position and orientation end-effector's path relative to manipulator's base, considering velocity performance," *Robotics and Computer-Integrated Manufacturing*, vol. 26, pp. 162–173, Apr. 2010.

[13] S. Stradovnik and A. Hace, "Task-oriented evaluation of the feasible kinematic directional capabilities for robot machining," *Sensors*, vol. 22, p. 4267, June 2022.

[14] Y. Xia, L. Zhao, Z. Liu, and K. Zhu, "Optimization of machining position for wheel hub polishing robot based on the kinematic index," *2022 8th International Conference on Control, Automation and Robotics, ICCAR 2022*, pp. 155–160, 2022.

[15] G. C. Vosniakos and E. Matsas, "Improving feasibility of robotic milling through robot placement optimisation," *Robotics and Computer-Integrated Manufacturing*, vol. 26, pp. 517–525, 2010.

[16] T. Weingartshofer, C. Hartl-Nesic, and A. Kugi, "Optimal tcp and robot base placement for a set of complex continuous paths," *Proceedings - IEEE International Conference on Robotics and Automation*, vol. 2021-May, pp. 9659–9665, 2021.

[17] R. K. Malhan, A. M. Kabir, B. Shah, and S. K. Gupta, "Identifying feasible workpiece placement with respect to redundant manipulator for complex manufacturing tasks," *2019 International Conference on Robotics and Automation (ICRA)*, pp. 5585–5591, May 2019.

[18] T. Yoshikawa, "Manipulability of robotic mechanisms," *The International Journal of Robotics Research*, vol. 4, pp. 3–9, June 1985.

[19] I. D. Marinescu, W. B. Rowe, B. Dimitrov, and H. Ohmori, "5 - forces, friction, and energy," in *Tribology of Abrasive Machining Processes (Second Edition)*, second edition ed., I. D. Marinescu, W. B. Rowe, B. Dimitrov, and H. Ohmori, Eds. Oxford: William Andrew Publishing, 2013, pp. 95–136.